Research Square

Preprints are preliminary reports that have not undergone peer review.
They should not be considered conclusive, used to inform clinical practice,
or referenced by the media as validated information.

Coexisting positive and negative ionospheric storms and large-scale traveling ionospheric disturbances over China during the October 2024 geomagnetic storm

Sheng Wang
Wuhan University
Yibin Yao
ybyao@whu.edu.cn
Wuhan University
Liu Lei
Wuhan University
Jun Tang
Kunming University of Science and Technology
Yuhan Gao
Wuhan University
Jintao Wang
Wuhan University

Research Article

Keywords: Positive and negative ionospheric responses, LSTIDs, DDEF, Geomagnetic storm

Posted Date: November 25th, 2026

DOI: https://doi.org/10.21203/rs.3.rs-11604184/v1

License: This work is licensed under a Creative Commons Attribution 4.0 International License.
Read Full License

Additional Declarations: No competing interests reported.

Coexisting positive and negative ionospheric storms and large-scale traveling ionospheric disturbances over China during the October 2024 geomagnetic storm

Sheng Wang[1]·Yibin Yao[1]·Lei Liu[1] Jun Tang[2] Yuhan Gao[1] Jintao Wang[1]

1 School of Geodesy and Geomatics, Wuhan University, Wuhan, China.

2 Faculty of Land Resources Engineering, Kunming University of Science and Technology, Kunming, China.

Corresponding authors: Yibin Yao (ybyao@whu.edu.cn); Lei Liu (leiliu@whu.edu.cn)

Abstract

This study combines ground-based GNSS observations, satellite measurements, geomagnetic data, and TIE-GCM simulations to investigate the evolution and driving mechanisms of positive and negative ionospheric storms and large-scale traveling ionospheric disturbances (LSTIDs) over China during the 10-11 October 2024 geomagnetic storm. (a) From the late main phase to the early recovery phase, a low-latitude positive storm coexisted with negative disturbances at higher latitudes, accompanied by enhancement and poleward expansion of the equatorial ionization anomaly (EIA) crest. Around 05:00-06:00 UT, the positive disturbance shifted to midlatitudes, while a negative storm developed at low latitudes. The negative storm was concentrated within 15°-35°N and intensified toward lower latitudes. Within 15°-25°N, the maximum VTEC depletion reached approximately 52 TECU, exceeding 60% of the background value, and the negative storm persisted for about 12.5 h; no sustained negative storm developed within 35°-45°N. COSMIC-2 profiles further revealed a transition from early electron density enhancement to deep depletion, accompanied by an increase in the F2 peak height. Mechanism analysis indicates that nighttime eastward disturbance electric fields and penetration electric fields under undershielding conditions enhanced the fountain effect, while equatorward winds lifted the F layer and reduced plasma loss, jointly producing the positive storm. During daytime, westward disturbance electric fields suppressed plasma supply to the EIA and, together with poleward winds, promoted the development of the negative storm. The absence of widespread O/N_2 depletion suggests that thermospheric compositional change was not the dominant driver of the low-latitude negative storm. (b) Five groups of equatorward-propagating LSTIDs were identified, with phase speeds of 397-662 m/s, periods of 50-64 min, and wavelengths of 1380-2383 km. Their occurrence broadly coincided with

enhancements in field-aligned currents and auroral electrojet activity, consistent with excitation by atmospheric gravity waves generated through high-latitude energy and momentum input. These results demonstrate the combined electrodynamic and neutral-atmospheric control of storm-time ionospheric responses and provide observational evidence for magnetosphere-ionosphere-thermosphere coupling over China.

Keywords Positive and negative ionospheric responses, LSTIDs, DDEF, Geomagnetic storm

Introduction

The electron density distribution in the low-latitude ionosphere is closely linked to the equatorial fountain effect. The equatorial upward E×B drift and subsequent plasma diffusion along magnetic field lines together produce the EIA, so electric-field variations can affect both low-latitude electron density and its latitudinal distribution (Fejer 2011). During geomagnetic storms, the prompt penetration electric field (PPEF) and the disturbance dynamo electric field (DDEF) are two major electric fields that modify this transport process, with distinct sources and response timescales (Fejer 2002). The PPEF is closely associated with variations in magnetospheric convection and shielding conditions: under daytime undershielding conditions, eastward electric-field disturbances can enhance the equatorial upward drift, promoting enhancement and poleward expansion of the EIA; under overshielding conditions, westward disturbances can suppress the fountain effect (Veenadhari et al. 2010). High-latitude heating and momentum input can also alter thermospheric circulation (Blanc and Richmond 1980). The resulting neutral-wind disturbances generate the DDEF through dynamo action, and this field can continue to affect low-latitude transport after high-latitude activity weakens (Scherliess and Fejer 1997). The DDEF is typically westward during the day and eastward at night, although its actual response also depends on local time, season, and longitude (Fejer et al. 2008). The superposition of these rapid electrodynamic responses and slower thermospheric adjustments leads to distinct low-latitude ionospheric behavior during the main and recovery phases.

Positive and negative ionospheric storms manifest as enhancements and depletions, respectively, in electron density or TEC relative to the background; their amplitude, duration, and spatial distribution depend on the balance among plasma production, loss, and transport (Buonsanto 1999; Mendillo 2006). In addition to electric-field-induced changes in fountain transport, equatorward neutral winds can raise the F layer and slow plasma diffusion to lower altitudes, thereby reducing chemical loss and favoring the

formation of positive storms (Balan et al. 2009; Lu et al. 2008). Negative storms are often associated with changes in thermospheric composition, heating-induced upwelling at high latitudes produces air enriched in molecular species, which is transported to lower latitudes by storm-time circulation and background winds, reducing the O/N_2 ratio and enhancing plasma loss (Fuller-Rowell et al. 1996). Daytime westward disturbance electric fields can also weaken the equatorial upward drift and plasma supply to the EIA crest, indicating that changes in plasma transport can also contribute to low-latitude depletion (Bagiya et al. 2011). Multi-instrument observations have shown that positive and negative storm responses vary markedly with longitude, latitude, and local time (Astafyeva et al. 2015). Studies of the October 2024 geomagnetic storm also reported ionospheric depletion lasting more than a day, indicating that electron density anomalies can persist well into the recovery phase (Pierrard et al. 2025). However, multiple mechanisms can produce TEC decreases, and depletion signatures alone are insufficient to determine the relative contributions of these mechanisms. Therefore, continuous TEC observations, vertical electron density profiles, and information on thermospheric composition, winds, and electric fields are needed to explain the development, persistence, and latitudinal differences of low-latitude negative storms during the recovery phase.

Ionospheric responses during geomagnetic storms also include traveling ionospheric disturbances (TIDs), whose excitation and propagation are major research topics. Based on their temporal and spatial scales, TIDs are generally classified into medium-scale TIDs (MSTIDs) and LSTIDs, which have different driving sources (Hocke and Schlegel 1996). Atmospheric gravity waves (AGWs) are an important source of MSTIDs, while some nighttime midlatitude MSTIDs also involve the Perkins instability and its electrodynamic coupling with sporadic E layers. Storm-time LSTIDs are often associated with auroral Joule heating, particle heating, and ion drag. These energy and momentum inputs can excite large-scale thermospheric disturbances, which, through ion-neutral coupling, appear as electron density fluctuations propagating toward middle and low latitudes (Hunsucker 1982). A statistical study over Europe found that the amplitudes of equatorward-propagating LSTIDs were correlated with auroral electrojet activity, providing observational support for high-latitude forcing (Borries et al. 2009). Two-dimensional GPS imaging over China further revealed the equatorward propagation of LSTIDs and their attenuation at low latitudes (Ding et al. 2012). Global observations of the October 2024 geomagnetic storm also revealed regional differences in LSTID activity during the same storm (Paul et al. 2025). However, detecting equatorward propagation in a given region is insufficient to identify the source

regions of individual disturbance groups. For multiple disturbance groups spanning the main and recovery phases, it is necessary to determine the occurrence time, propagation direction, and speed of each group and to assess their possible drivers by considering the location and intensity of high-latitude activity in the relevant sectors, together with the propagation delay between that activity and the observed disturbances.

Taking the 10-11 October 2024 geomagnetic storm as a case study, this paper investigates the mechanisms governing the evolution of positive and negative ionospheric storms over China and TID propagation during the main and recovery phases. BDS-GEO observations and the interquartile range (IQR) method are used to identify TEC anomalies at different latitudes. These observations are combined with regional TEC variations from CMONOC, Swarm in situ electron density measurements, and COSMIC-2 electron density profiles to characterize the amplitude, duration, spatial extent, and vertical structure of the positive and negative storms. Furthermore, GUVI O/N_2 measurements, the H-component magnetic field difference between DLT and BMT, and thermospheric neutral winds from TIE-GCM simulations are used to evaluate the roles of compositional changes, neutral-wind transport, and disturbance electric fields in the formation and transition of the positive and negative storms. For the TID analysis, DTEC maps and time-latitude profiles from CMONOC are used to analyze the propagation structures and apparent phase speeds of five groups of disturbances. The TID characteristics are further compared with AMPERE-derived field-aligned currents (FACs) in the East Asian sector and auroral electrojet activity to examine their possible links to high-latitude forcing.

Data and Method

Data source

This study uses two ground-based GNSS datasets for 8-14 October 2024: one from 247 CMONOC stations across China, and the other from nine GNSS stations across East Asia capable of receiving BDS-GEO signals, including five MGEX stations and four iGMAS stations. Both datasets have a sampling interval of 30 s. The nine BDS-GEO stations span geographic latitudes of approximately 22°-48°N; their station locations, satellite PRNs, and ionospheric pierce point (IPP) coordinates are listed in Table 1. In addition, fluxgate magnetometer observations from the BMT and DLT stations at 1 min resolution are used to analyze low-latitude electrodynamic variations. The spatial distribution of these ground-based stations and representative IPPs is shown in Figure 1.

Solar wind parameters and geomagnetic indices were obtained from the OMNIWeb database of

NASA's Goddard Space Flight Center, including IMF Bz, solar wind speed (Vsw), proton number density (Np), SYM-H, AE, AL, AU, Dst, Kp, and F10.7; the IEF-Ey was also used to support the analysis of external electrodynamic forcing. FAC data were obtained from the AMPERE project at the Johns Hopkins University Applied Physics Laboratory. Northern Hemisphere radial current density data were used, and area-weighted integration was performed separately for the upward and downward components to characterize high-latitude current activity (Anderson et al. 2014). Thermospheric O/N_2 data were taken from the TIMED/GUVI product to examine changes in thermospheric composition (Christensen et al. 2003). Storm-time COSMIC-2 electron density profiles were compared with reference profiles at similar locations and local times. Transport conditions were analyzed using TIE-GCM neutral wind fields at 350 km altitude (Qian et al. 2014).

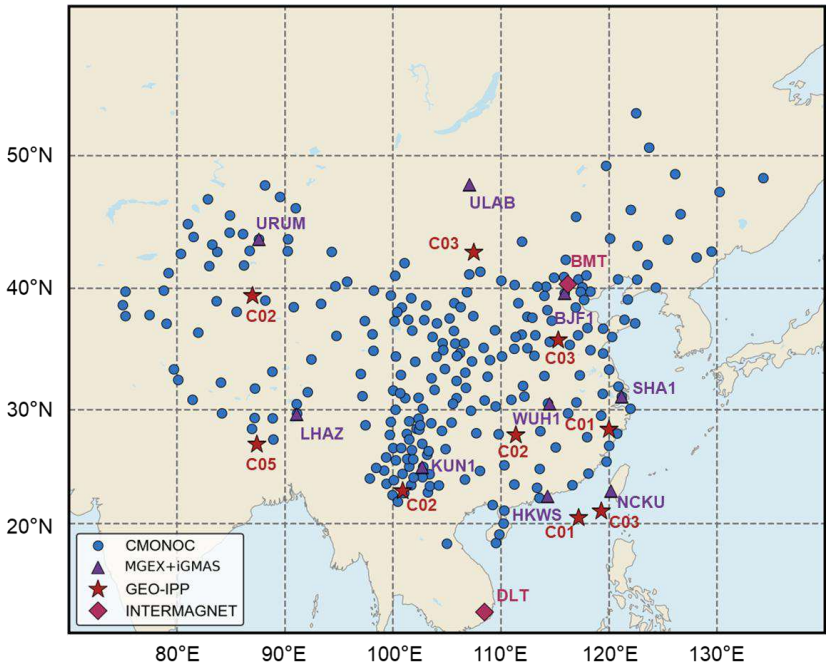

Fig.1 Spatial distribution of the multi-source GNSS ground stations. Blue dots denote CMONOC stations, purple triangles denote GNSS stations equipped with BDS-GEO receivers, red stars denote the ionospheric pierce points of these stations projected onto the Earth's surface, and magenta diamonds denote magnetometer stations

Ionospheric Disturbance and Electrodynamic Analysis Methods

In this study, the IQR method is used to identify storm-time TEC anomalies in BDS-GEO observations. Following the approach of Sun et al. (2026), anomaly bounds are constructed from the median and interquartile range using observations over 16 days from 20 September to 5 October 2024 as the background reference. For each station-satellite pair, TEC values at the same UT epoch on each reference day are assembled into a sample, and the first quartile (Q_1) and third quartile (Q_3) are calculated at 30 s intervals. Missing values are excluded from the calculations. The anomaly-detection bounds are defined

as follows:

$$\begin{aligned} IQR &= Q_3 - Q_1 \\ LB &= Q_1 - k \times IQR \\ UB &= Q_3 + k \times IQR \end{aligned} \tag{1}$$

where LB and UB denote the lower and upper detection bounds, respectively, and k is set to 1.5 in this study. When the background and detection bounds defined above are applied to the observations from 8-14 October 2024, TEC values below the lower bound or above the upper bound are identified as negative or positive anomalies, respectively.

Table 1 Station & IPP configuration of the BDS-GEO monitoring network

Station	Geographic coordinates	Geomagnetic coordinates	PRN	IPP geographic coordinates
BJF1	115.9°E, 39.6°N	173.9°W, 28.8°N	C03	115.3°E, 35.8°N
ULAB	107.1°E, 47.9°N	178.3°E, 36.9°N	C03	107.5°E, 42.8°N
URUM	87.6°E, 43.8°N	161.7°W, 34.4°N	C02	87.0°E, 39.4°N
WUH1	114.5°E, 30.5°N	175.0°W, 19.7°N	C02	111.4°E, 27.8°N
SHA1	121.2°E, 31.1°N	164.2°W, 21.8°N	C01	120.0°E, 28.3°N
LHAZ	91.1°E, 29.6°N	164.9°E, 20.3°N	C05	87.4°E, 27.0°N
NCKU	120.2°E, 22.9°N	167.8°W, 13.5°N	C03	119.3°E, 21.1°N
KUN1	102.7°E, 25.0°N	175.6°E, 15.4°N	C02	100.9°E, 22.9°N
HKWS	114.3°E, 22.4°N	174.9°W, 11.5°N	C01	117.2°E, 20.5°N

To extract TID propagation structures, geometry-free combinations were constructed from dual-frequency GPS carrier-phase observations from CMONOC to obtain relative slant total electron content (STEC; Krypiak-Gregorczyk and Wielgosz 2018). A 30° elevation cutoff was applied, and continuous arcs were delineated based on loss of lock, cycle slips, and data gaps; only valid arcs with durations of at least 10 min were retained. Following Ding et al. (2007), the background variation in slant TEC was removed by fitting and subtracting a quadratic polynomial within each valid arc. The resulting perturbations were then mapped to vertical TEC perturbations using a single-layer model with an effective height of 450 km:

$$DTEC(t) = [STEC_{phase} - P_2(t)] \cos z' \tag{2}$$

where $P_2(t)$ is the quadratic polynomial representing the background within each arc, and z' is the

zenith angle at the IPP. The DTEC values from all valid arcs were organized according to IPP location and time to construct two-dimensional distributions and time-latitude profiles averaged over longitude bands. The occurrence time and propagation parameters (apparent phase speed, period, and wavelength) of each disturbance group were extracted from the phase fronts in the profiles and two-dimensional distributions. The phase speed was determined from the slopes of the phase fronts, while the period and wavelength were estimated from the temporal and spatial separations between adjacent fronts (Tsugawa et al. 2004).

Following previous studies that used two-station H-component differences to characterize equatorial electrojet variations (Anderson et al. 2002; Balan et al. 2010), observations from DLT and BMT are used to construct an H-component difference series:

$$D_H(t) = H_{DLT}(t) - H_{BMT}(t) - \overline{H_{DLT}} - \overline{H_{BMT_{ref}}} \quad (3)$$

where H_{DLT} and H_{BMT} are the horizontal magnetic field components at the two stations, respectively; the overbar denotes the reference-day mean; and D_H is expressed in nT. The reference-day diurnal variation of D_H is also retained as a baseline for evaluating daytime enhancement or suppression during the storm.

Results

Variations in Geomagnetic Indices During the Storm

A fast CME that erupted on 9 October 2024 arrived at Earth on 10 October, triggering this superstorm (Singh et al. 2025). Figure 2 shows the interplanetary parameters and geomagnetic indices for 8-14 October. On the morning of 10 October, geomagnetic activity had decreased from the recovery phase of the preceding storm to relatively quiet levels. At approximately 15:20 UT, the CME shock arrived and caused a storm sudden commencement (SSC; Kataoka et al. 2025), with SYM-H rising rapidly from −8 to +78 nT. Vsw increased from approximately 460 to 843 km/s, and the proton number density reached a maximum of 42 cm^{-3}. Subsequently, IMF Bz fluctuated between northward and southward; SYM-H generally decreased; and the storm entered its main phase. After approximately 22:30 UT, IMF Bz became strongly southward, reached a minimum of −47.7 nT at 22:40 UT, and remained strongly southward until the morning of 11 October. SYM-H briefly dropped to −390 nT at 23:14 UT on 10 October; this transient negative excursion was associated with a sudden decrease in solar wind dynamic pressure (Rai et al. 2026) and did not mark the end of the main phase. After a brief rebound, SYM-H decreased again, reaching the main-phase minimum of −346 nT at 01:22 UT on 11 October, and then generally increased as the storm gradually entered the recovery phase. Dst reached a minimum of −333

nT at 01:00 UT on 11 October, and Kp reached 8.7 between 21:00 and 24:00 UT on 10 October. AE increased rapidly after the SSC, peaking at 4274 nT at 15:53 UT on 10 October, and exhibited multiple significant enhancements during the main and early recovery phases. After approximately 09:30 UT on 11 October, IMF Bz became generally northward, AE gradually declined, and Dst continued to recover, reaching above −30 nT by the night of 13 October. During the study period, F10.7 ranged from 181 to 224 sfu, indicating high solar activity.

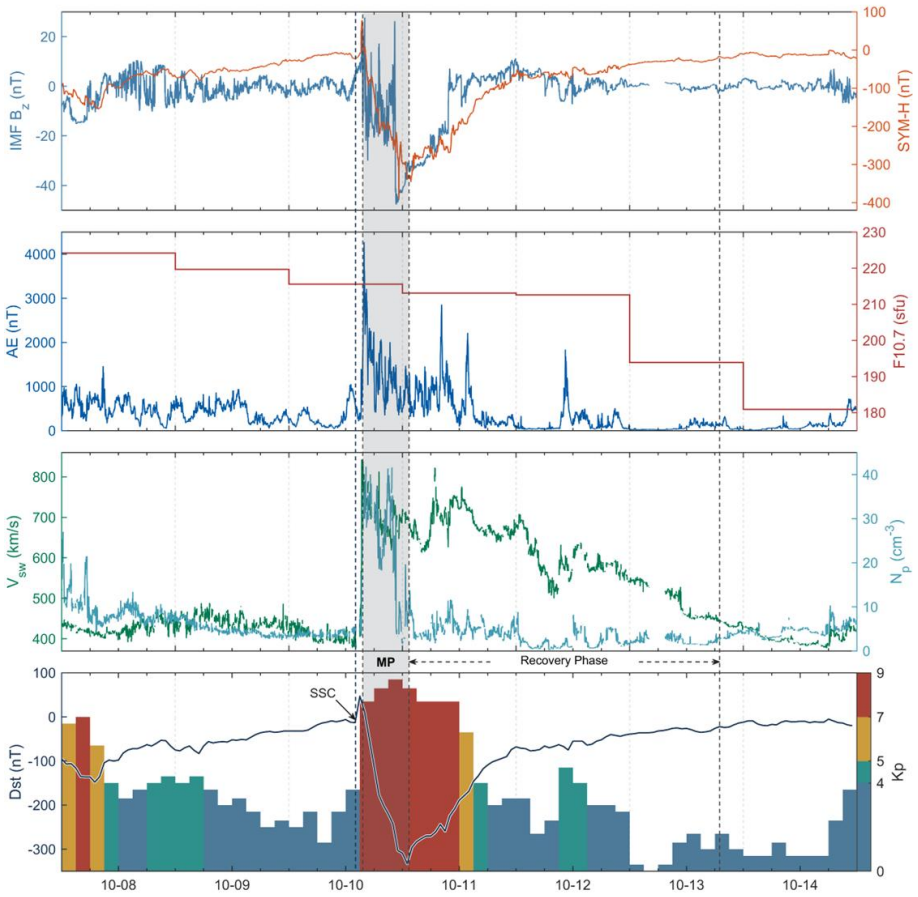

Fig. 2 Interplanetary and geomagnetic conditions during 8-14 October 2024. From top to bottom: IMF-Bz component and SYM-H index; AE index and F10.7; Vsw and proton density (Np); Dst index and Kp index. The vertical dashed lines indicate the storm sudden commencement (SSC), main phase (MP, shaded area), and recovery phase intervals

Spatiotemporal Evolution of Positive and Negative Ionospheric Storms

Figure 3 shows the BDS-GEO VTEC time series and IQR anomaly detection results for representative stations in three latitudinal bands, arranged in descending order of IPP latitude: 35°-45°N (ULAB, 42.8°N), 25°-35°N (WUH1, 27.8°N), and 15°-25°N (KUN1, 22.9°N). Figure 3(d) presents Vsw and SYM-H to indicate the storm phases. The IQR method is used to detect VTEC anomalies, and observations below the lower detection bound are classified as negative anomalies. The VTEC depletion relative to the background median and the magnitude of exceedance below this bound are used to

quantify disturbance intensity and anomaly significance, respectively, while the duration of continuous excursions below this bound is used to quantify persistence.

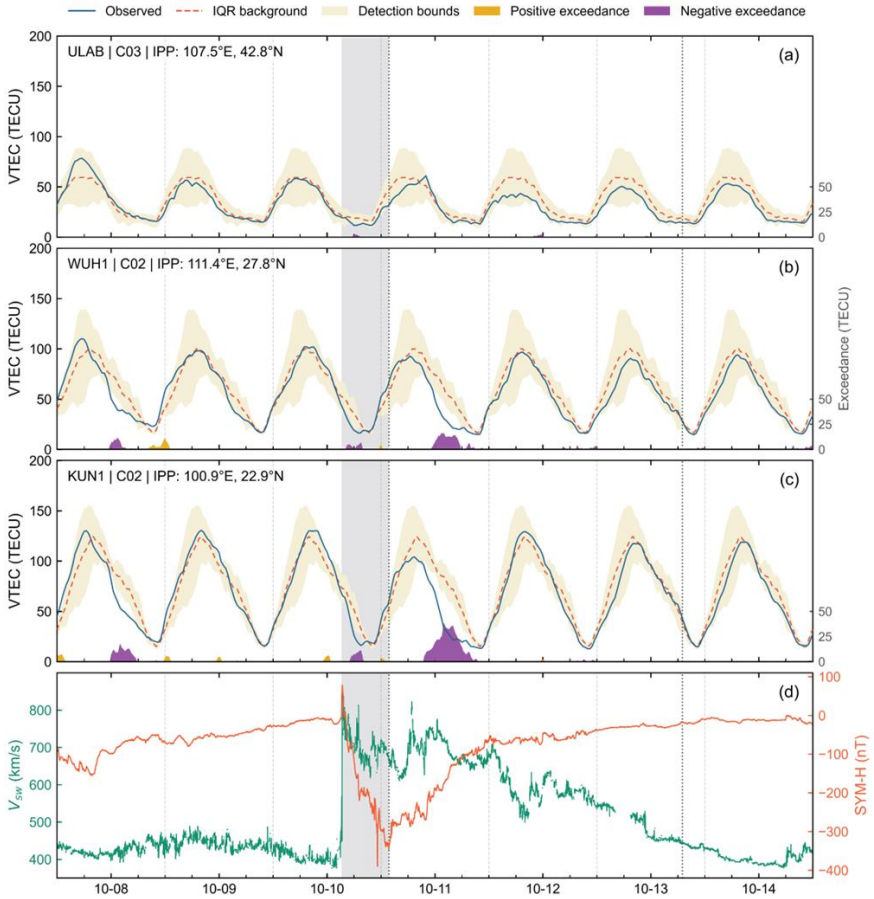

Fig. 3 Latitudinal response differences of BDS-GEO VTEC and IQR anomaly detection results during 8-14 October 2024. The top three panels, from top to bottom, show the representative stations ULAB, WUH1, and KUN1, respectively; the station, satellite PRN, and ionospheric pierce point coordinates are labeled in the upper-left corner of each panel; the bottom panel shows Vsw (green, left axis) and the SYM-H index (brown, right axis)

The 35°-45°N band showed the weakest disturbances (Figure 3a). On 11 October, the maximum VTEC depletion at ULAB relative to the background was 16.7 TECU (28.2%, 04:00 UT), but the magnitude of exceedance below the lower bound was only 0.9 TECU, and no persistent anomaly developed. On 12 October, the depletion increased further, but the exceedance remained small and intermittent. Overall, this band exhibited only weak negative deviations from the background, with no significant negative anomalies. The 25°-35°N band showed significant negative anomalies (Figure 3b). On 11 October, the maximum VTEC depletion at WUH1 reached 31.8 TECU, equivalent to 46% of the contemporaneous background value, and the maximum exceedance below the lower bound was 16.3 TECU. The continuous negative anomaly began between 10:00 and 11:00 UT and persisted for 6.9 h. On 12 October, the negative anomaly weakened markedly. The 15°-25°N band showed the strongest negative anomaly (Figure 3c). KUN1 exhibited a short-lived negative anomaly during the main phase on 10

October. On 11 October, the negative anomaly intensified markedly during the recovery phase, with a maximum VTEC depletion of 51.8 TECU (around 14:00 UT), exceeding 60% of the contemporaneous background value. The continuous negative anomaly began at approximately 09:20 UT and persisted for about 12.5 h. On 12 October, the strong negative anomaly had largely ended, leaving only weak intermittent exceedances.

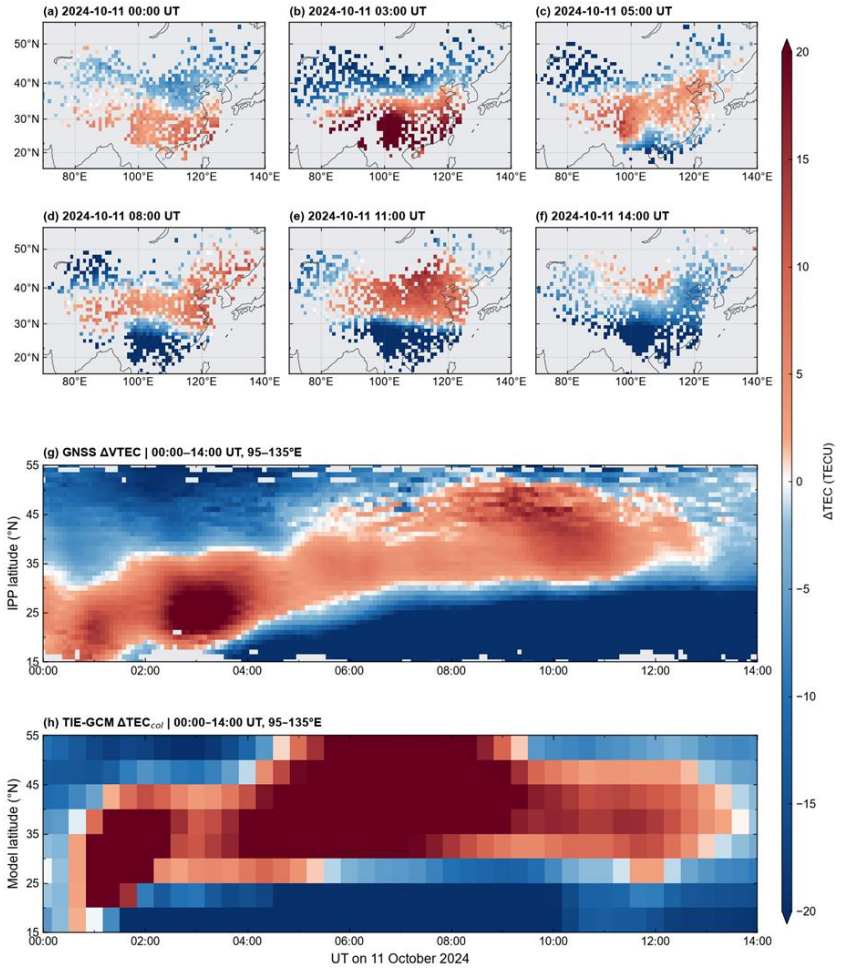

Fig. 4 Spatial distribution of ΔTEC ($\Delta TEC = TEC_{storm} - TEC_{quiet}$) and its time-latitude evolution over China and adjacent regions during the recovery phase on 11 October 2024. (a-f) Spatial distributions at 00:00-14:00 UT, respectively; (g) time-latitude profile averaged over the 95°-135°E longitude band during 00:00-14:00 UT; (h) time-latitude profile from the corresponding TIE-GCM simulation (grid resolution 2.5°×5°)

The three stations exhibit a clear latitudinal gradient: the intensity and persistence of the negative anomalies systematically increase with decreasing latitude, and significant negative storm responses are concentrated at 15°-35°N during the recovery phase. Notably, between 02:30 and 03:00 UT on 11 October, KUN1 and WUH1 showed positive deviations of +13.2 and +12.5 TECU, respectively, while ULAB showed a negative deviation during the same period, indicating a latitudinal coexistence of positive and negative deviations. However, the maximum positive deviations at KUN1 and WUH1 did

not exceed the upper IQR detection bound, and no significant positive anomalies were detected. To clarify the spatial extent and evolution of this pattern of coexisting positive and negative deviations, the analysis is extended from fixed GEO-IPP observations to regional CMONOC observations. ΔTEC maps and a time-latitude profile averaged over the 95°-135°E longitude band are constructed (Figure 4).

Figure 4 shows the evolution of the ΔTEC distribution over China from 00:00 to 14:00 UT (08:00-22:00 LT) on 11 October. The median VTEC from the quiet days of 3-5 October was used as the quiet-time reference for calculating ΔTEC. During 00:00-05:00 UT, positive and negative responses coexisted at different latitudes, a significant positive response occurred at 20°-35°N, with a peak of approximately 29 TECU located at the latitude of the northern EIA crest, while the response north of 40°N was negative. Around 05:00-06:00 UT, the negative response region began expanding equatorward; the region south of 25°N became negative, and the depletion continued to deepen. Meanwhile, the positive response region expanded poleward, with its poleward boundary reaching approximately 50°N during 08:00-11:00 UT. The latitudinal distribution of the positive and negative responses was reversed during this period. After approximately 12:00 UT, the positive response region that had expanded poleward weakened, and by approximately 13:00 UT the positive storm had essentially disappeared. At 14:00 UT, the region south of 45°N was dominated entirely by negative responses, with the negative storm core located at 20°-30°N and ΔTEC values as low as approximately −50 TECU. Overall, the positive storm first disappeared at low latitudes around 05:00-06:00 UT; after expanding poleward, it persisted at midlatitudes until approximately 12:00-13:00 UT, and negative storm conditions subsequently dominated China.

The TIE-GCM simulation (Figure 4h) is qualitatively consistent with the observations, reproducing the coexistence of positive responses at low and middle latitudes and negative responses at high latitudes during 00:00-05:00 UT, the subsequent poleward expansion of the positive response region (extending to 45°-55°N during 04:00-12:00 UT), and the negative responses at low latitudes. The main differences are that the simulated positive response region is broader and persists longer. These differences may be related to the model grid resolution.

Figure 5 presents the in situ electron density (Ne) from Swarm A/C at approximately 09:50 UT on 11 October, together with its difference (ΔNe) relative to the 14 October reference day. The latitudinal distribution of ΔNe directly reveals the coexistence of positive and negative storm responses, with significant depletion at 15°-22°N, widespread enhancement at 22°-51°N, and weak depletion north of 51°N. The boundaries between the positive and negative regions are consistent with the latitudinal pattern

of GNSS ΔTEC at the same time.

To investigate variations in the vertical structure of the ionosphere during the storm, Figure 6 compares COSMIC-2 electron density profiles with quiet-day reference profiles at nearby locations. The three profiles at 02:55-06:21 UT show a gradual transition from enhancement to depletion: at 02:55 UT, NmF2 was enhanced by approximately 46% relative to the reference, and hmF2 was elevated by approximately 45 km, consistent with the low-latitude positive disturbance region shown in Figure 4 during the same period; at 04:12 UT, NmF2 was already slightly below the reference, and at 06:21 UT it was approximately 27% below the reference. In both of these profiles, hmF2 values remained approximately 29-32 km above the reference, with peak density depletion and peak height elevation occurring simultaneously. The three profiles at 12:04-17:40 UT show overall depletion, with NmF2 approximately 24%, 58%, and 81% below the reference, respectively, and the depletion deepening monotonically toward nighttime, corresponding to the negative-storm-dominated stage. Taken together, the profiles at different locations indicate that the transition from early enhancement to significant depletion during the recovery phase is consistent with the overall process revealed by CMONOC: the fading of the low-latitude positive storm and the gradual development of the negative storm. These profiles therefore provide complementary vertical-structure evidence for the evolution of positive and negative storms during the recovery phase.

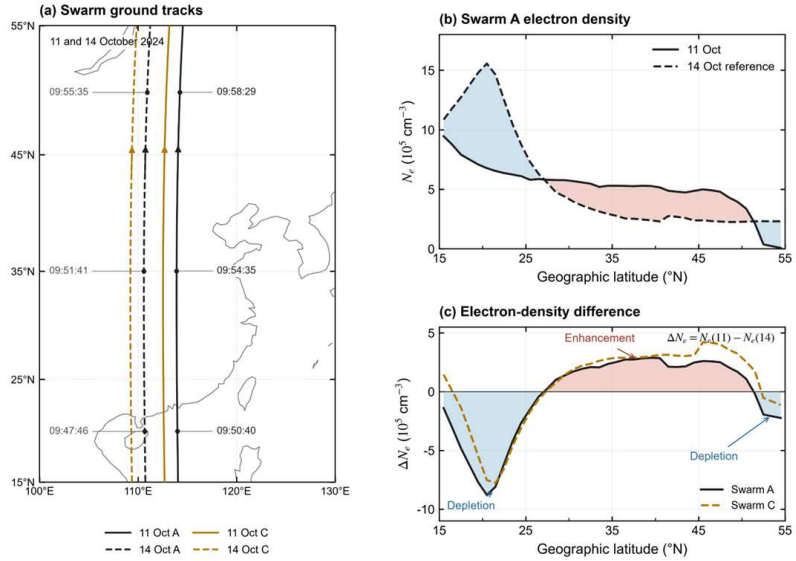

Fig. 5 Swarm observations at approximately 09:50 UT on 11 Oct 2024: (a) ground tracks of Swarm A and C on 11 and 14 Oct; (b) Swarm A electron density profiles on the storm day (11 Oct) and qu iet day (14 Oct); (c) storm-minus-quiet electron density differences for Swarm A and C

Figure 7 shows the thermospheric O/N_2 distribution observed by GUVI during 9-14 October. During the recovery phase on 11 October, O/N_2 at low and middle latitudes in the study region was generally

enhanced, with a relatively continuous region of high values forming around 20°-40°N and with local values reaching approximately 1.1-1.3. Meanwhile, O/N_2 at higher latitudes decreased markedly, showing a different latitudinal response. On 12 October, O/N_2 at low and middle latitudes remained relatively high, and the enhancement gradually weakened over the following two days.

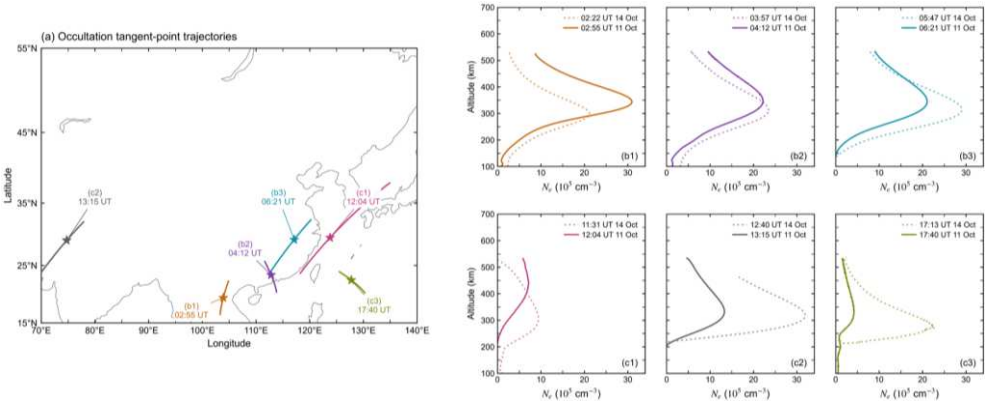

Fig. 6 Comparison of COSMIC-2 electron density profiles during the recovery phase on 11 October 2024 with reference profiles from 14 October 2024. (a) Selected occultation tangent-point trajectories and representative locations. (b1-b3) Profiles observed at 02:55, 04:12, and 06:21 UT on 11 October, respectively. (c1-c3) Profiles observed at 12:04, 13:15, and 17:40 UT on 11 October, respectively. Solid and dotted lines indicate storm-time profiles and reference profiles at nearby locations, respectively

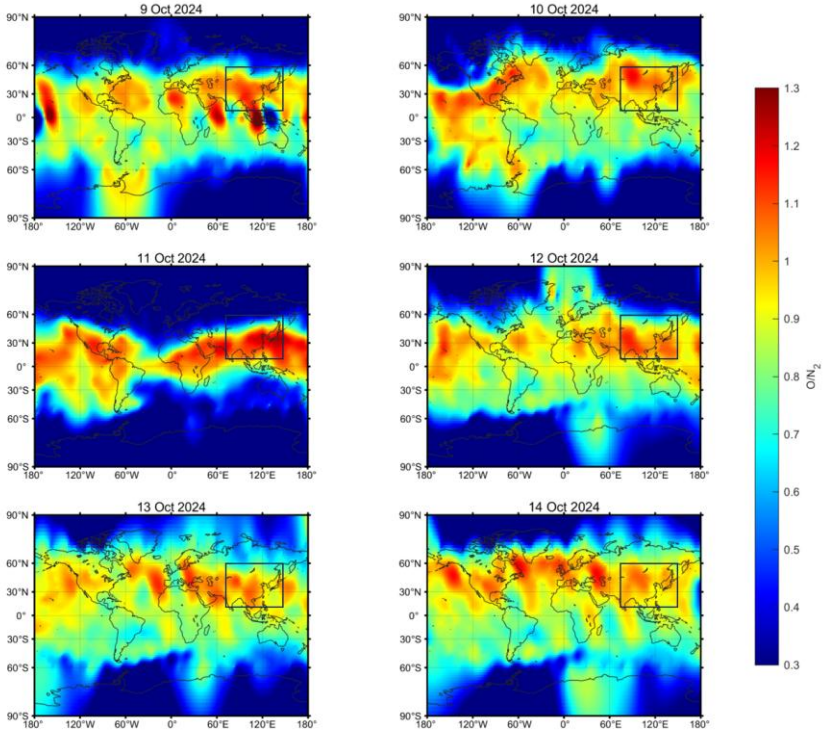

Fig. 7 Spatial distribution of thermospheric O/N_2 observed by TIMED/GUVI during 9-14 October 2024. Each panel corresponds to the global distribution on the respective day, and the rectangular box marks the East Asian region of interest in this study

Notably, on 11 October, the enhancement in low-latitude O/N_2 coincided with the depletion of VTEC and electron density. The negative storm region was not accompanied by widespread O/N_2

reduction, indicating that thermospheric compositional depletion alone cannot readily explain the low-latitude negative storm in this region. The specific cause is discussed further below.

Propagation Characteristics of LSTIDs During the Storm

The preceding analysis has described the enhancement and depletion of background TEC and their regional evolution during the geomagnetic storm. To identify the propagating disturbances superimposed on this background, this section uses DTEC derived from CMONOC observations to analyze the two-dimensional spatial structures of the disturbances and to estimate their propagation parameters from time-latitude profiles. Figure 8 shows the spatial distributions of five groups of TIDs at successive times on 10-11 October.

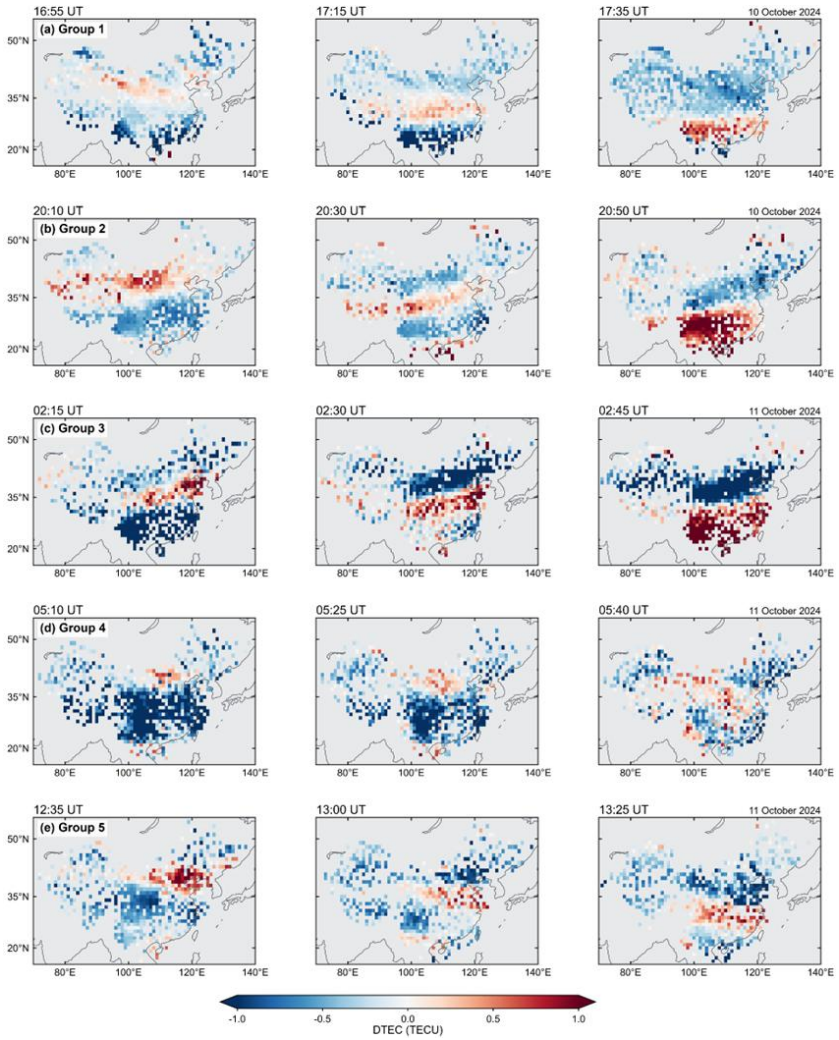

Fig. 8 Two-dimensional propagation evolution of five groups of LSTIDs based on CMONOC observations. (a-e) correspond to Groups 1-5, respectively, with the specific times labeled above each panel. Red and blue denote positive and negative disturbances, respectively

Groups 1 and 2 occurred during the main phase (Figures 8a, b). For Group 1 (16:55-17:35 UT on 10 October), the positive disturbance band first appeared at about 38°N and then moved continuously

southward, reaching about 23°N by the final time step, while the region north of 30°N became a broad negative disturbance. Group 2 (20:10-20:50 UT on 10 October) had the strongest positive disturbance: the disturbance band moved southward from about 41°N, and by the final time step a significant low-latitude positive disturbance region formed at about 23°-28°N, with negative disturbances appearing to its north. Groups 3-5 occurred during the recovery phase (Figures 8c-e). For Group 3 (02:15-02:45 UT on 11 October), the alternating positive and negative phase structure was the clearest: the positive disturbance band gradually moved southward from about 38°N, with its southern end reaching about 23°N, and the negative disturbance was correspondingly located to its north. For Group 4 (05:10-05:40 UT on 11 October), the negative phase dominated and the positive disturbance was weaker; the disturbance region moved southward from about 44°N to about 32°N. For Group 5 (12:35-13:25 UT on 11 October), the distribution was relatively scattered, but a positive disturbance band moving southward from about 41°N to about 29°N was still identifiable.

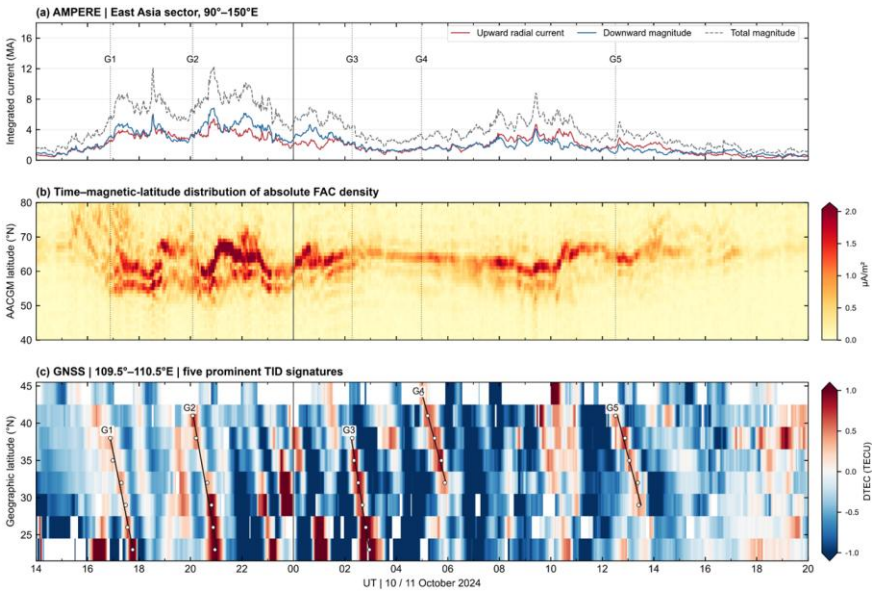

Fig. 9 Temporal comparison between East Asian field-aligned currents and GNSS LSTID characteristics from 14:00 UT on 10 October to 20:00 UT on 11 October 2024. From (a)-(c): the AMPERE integrated currents in the East Asian sector; the time-magnetic latitude distribution of the absolute current density; and the time-geographic latitude distribution of DTEC within 110° ± 0.5°E; open circles denote the arrival times of observed positive peaks; the black solid line is the fit to the arrival times at multiple latitudes; G1-G5 denote the five groups of TIDs

Figure 9 compares the five TID groups with FAC activity in the East Asian sector. Figure 9a shows the evolution of the integrated FAC over this sector. On 10 October, the upward and downward currents generally intensified in phase, with strong, continuously fluctuating activity persisting during 17-23 UT. The sum of their magnitudes reached peaks of 12.06 and 12.27 MA at 18:33 UT and 20:55 UT, respectively. In the early hours of 11 October, the current activity weakened overall, although local peaks

of approximately 6.96 and 6.48 MA still occurred at 00:39 UT and 01:23 UT, respectively; the activity then strengthened again during 07-11 UT. Figure 9b shows that the stronger FAC activity was mainly concentrated at AACGM magnetic latitudes of approximately 55°-70°N, and that its intensity and latitudinal distribution underwent marked changes during the geomagnetic storm, reflecting the persistent disturbance and spatial reorganization of high-latitude electrodynamics.

Figure 9c shows the DTEC time-latitude profile within the longitude band of 110° ± 0.5°E, in which five groups of southward-propagating disturbances can be identified: G1 and G2 occurred at 16:53-17:45 UT and 20:05-20:57 UT on 10 October, respectively, and G3-G5 occurred at 02:17-02:57, 04:59-05:53, and 12:31-13:25 UT on 11 October, respectively. For each group, the arrival times of the positive phase peaks were delayed at lower latitudes, forming tracks that slope downward with increasing time and indicating that the disturbances propagated equatorward overall. The trackable ranges of G1-G3 extended from 38°N, 41°N, and 38°N to 23°N, respectively, and those of G4 and G5 were 44°N-32°N and 41°N-29°N, respectively. The meridional phase speeds obtained by fitting the phase arrival times at multiple latitudes were approximately 397-662 m/s (Table 2). Combined with periods of about 50-64 min and wavelengths of 1380-2383 km, all five groups of disturbances are classified as LSTIDs. Although G1 had a relatively small amplitude, its coherent phase structure still advanced continuously southward, exhibiting clear propagation characteristics.

Table 2. Occurrence times and propagation parameters of five LSTID groups during the geomagnetic storm of 10-11 October 2024

LSTID groups	Occurrence time (UT)	Propagation direction	Velocity (m/s)	Period (min)	Wavelength (km)	Affected latitude
Group 1	10th 16:53	Southward	523	50	1570	23°N-38°N
Group 2	10th 20:05	Southward	599	62	2228	23°N-41°N
Group 3	11th 02:17	Southward	662	60	2383	23°N-38°N
Group 4	11th 04:59	Southward	397	58	1380	32°N-44°N
Group 5	11th 12:31	Southward	403	64	1550	29°N-41°N

The timing relationships between the five disturbance groups and FAC enhancements are not consistent among the groups. G2, G3, and G5 occurred approximately 1.5-2 h after the strong high-latitude disturbance peak during the main phase, the local enhancement during the recovery phase, and the morning secondary enhancement, respectively. Using the observed apparent phase speeds, propagation from the auroral oval to the latitudes where the disturbances appeared is estimated to take about 0.5-2 h (Lyons et al. 2019), consistent with these lag times. This timing relationship supports the interpretation that auroral energy injection excited these three LSTID groups. In contrast, G1 occurred during the rising phase of FAC activity, before the first peak, and G4 occurred during the interval of low

activity between two enhancements. Neither disturbance followed a preceding FAC peak, so this mechanism cannot fully account for their triggering. The possible source mechanisms of the five disturbance groups are further discussed in the Discussion.

Discussion

This section focuses on the evolution mechanisms of the positive and negative ionospheric storms and the driving mechanisms of the five LSTID groups during this geomagnetic storm. Observations show that the positive storm appeared early on 11 October, accompanied by enhancement and poleward expansion of the EIA crests, whereas the negative storm was concentrated at 15°-35°N, with depletion intensifying toward lower latitudes. The GUVI observations for this event do not show widespread O/N_2 reduction in the negative storm region; therefore, the role of transport processes must be examined further.

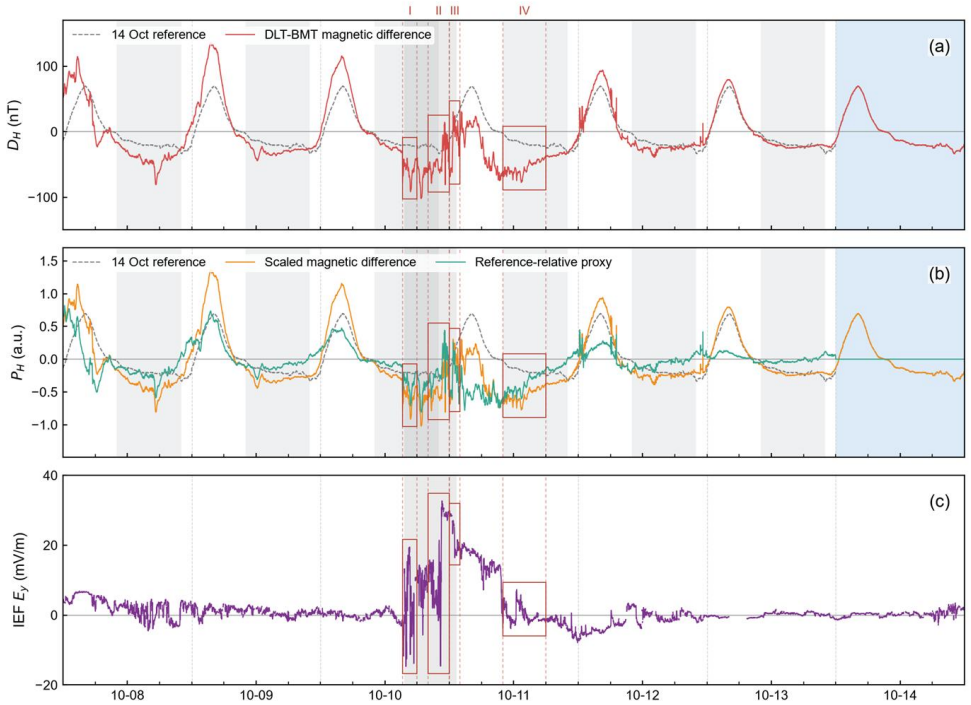

Fig. 10 Temporal variations of (a) D_H, (b) P_H, and (c)IEF-Ey during 8-14 October 2024. The light blue areas denote the selected quiet-day references, and the cyan curves are the disturbance proxies; in (a) and (b), the light gray shading indicates nighttime periods (~10:00-22:00 UT, corresponding to ~18:00-06:00 LT), the light blue shading on the right marks the quiet-day reference period, and the red boxes mark the disturbance events (I-IV) discussed in the text

Figure 10 presents D_H, a magnetic indicator derived from the two-station H-component difference during daytime, which serves to diagnose suppressed daytime electrodynamics. D_H is defined relative to the quiet-day reference of 14 October, and its weakening and reversal reflect changes in the disturbance field. From 02:00 to 05:00 UT on 11 October, the median D_H was approximately 10 nT, well below the quiet-day reference value of approximately 62 nT, indicating the presence of a westward disturbance

field that partially offset the background eastward field. From 05:00 to 08:00 UT, D_H became predominantly negative, indicating further suppression of the daytime low-latitude magnetic response; this is consistent with an enhanced contribution from the westward disturbance electric field, and the electric field inferred from D_H was correspondingly lower than the reference. Importantly, during the same period, IMF Bz remained southward and IEF Ey was generally positive. If the penetration electric field had dominated the daytime low latitudes, it should have produced an eastward disturbance and enhanced the low-latitude currents, whereas the observed D_H showed a sustained weakening and even a reversal. This westward disturbance field persisted for approximately 6 h, consistent with the typical daytime westward polarity and time scale of the DDEF (Scherliess and Fejer 1997).

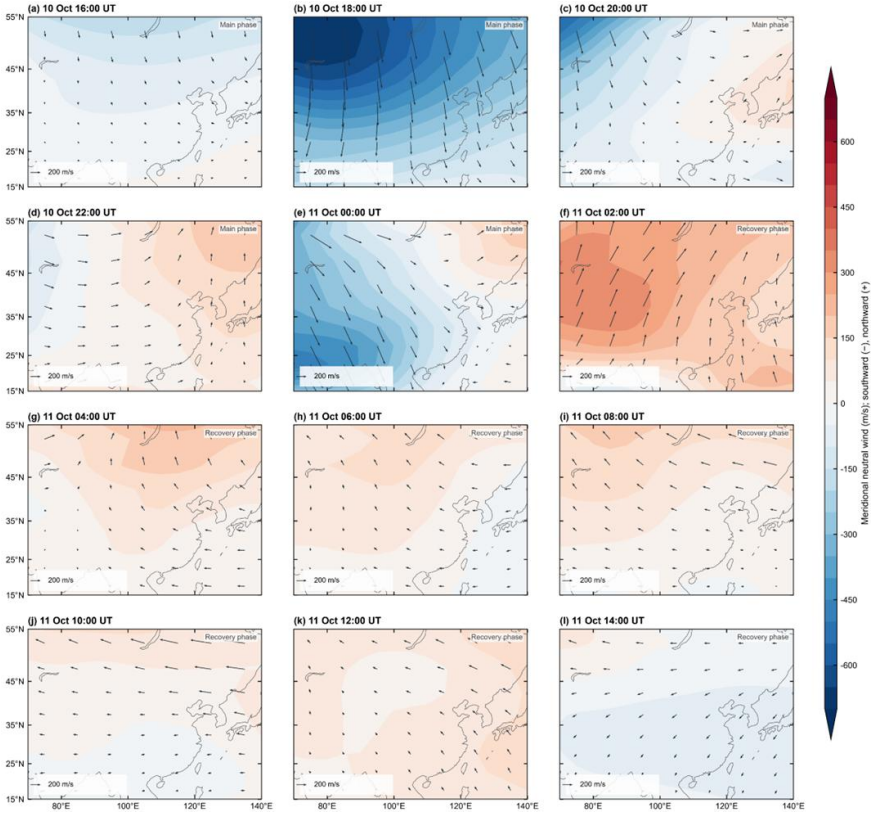

Fig. 11 Horizontal neutral wind fields at an altitude of 350 km simulated by TIE-GCM during 10-11 October 2024. Panels (a-e) show the main phase, and panels (f-l) show the recovery phase. Arrows indicate horizontal wind vectors, with a reference vector of 200 m s^{-1} in the lower-left corner of each panel. Colors represent the meridional component of the neutral wind, with red and blue indicating northward (positive) and southward (negative) flow, respectively

Figure 11 shows the meridional wind field at 350 km altitude from TIE-GCM simulations. During the early main phase, winds in the study region were weak. At 18:00 UT on 10 October, high-speed equatorward winds appeared widely over China. From 22:00 UT on 10 October to 00:00 UT on 11 October, the wind direction changed repeatedly. By 02:00 UT on 11 October, during the early recovery phase, a broad-scale poleward flow had developed, gradually weakening during the daytime on 11

October. In the Northern Hemisphere, poleward winds drive plasma downward along magnetic field lines and enhance recombination loss (Lu et al. 2008). At the same time, storm-time circulation can generate low-latitude disturbance electric fields through dynamo action, which are typically westward during the day and eastward at night (Blanc and Richmond 1980; Fejer et al. 2008). The close temporal relationship between the wind-field reorganization and the establishment of the negative storm indicates that low-latitude transport conditions underwent substantial changes.

The formation of the positive storm can be attributed to the combined effects of electric fields and winds from the night of 10 October to the early morning of 11 October. The nighttime eastward component of the disturbance electric field, together with the penetration electric field associated with undershielding during the Bz fluctuation period, strengthened the fountain effect and drove the enhancement of the EIA crest (Fejer 2011; Tsurutani et al. 2004). During the same period, two equatorward wind surges lifted the F layer at midlatitudes and reduced recombination loss, allowing plasma to be retained. The mechanism by which equatorward wind uplift and electric-field enhancement jointly produce low-latitude positive storms is well established (Balan et al. 2009, 2010; Lu et al. 2008). After 05:00-06:00 UT, the enhancement region shifted northward and persisted at midlatitudes. Once the winds became poleward at 02:00 UT, their effects differed with magnetic inclination: at low latitudes, the poleward component of the wind along the nearly horizontal magnetic field lines was significant, transporting plasma to higher latitudes and contributing to the northward migration of the positive disturbance region, whereas at midlatitudes the downward field-aligned component dominated. The earlier uplift had placed the plasma at a higher altitude with a lower loss rate, so the enhancement decayed more slowly and persisted into the morning. Meanwhile, GUVI showed elevated O/N_2 in the study region, providing favorable compositional conditions for maintaining the enhancement. During the daytime, low latitudes transitioned to sustained depletion, and the positive response gradually declined. As indicated by the two-station magnetic difference described above, the daytime westward disturbance electric field suppressed the fountain effect, and the EIA crest weakened and contracted as its plasma supply was reduced, resulting in strong depletion at the crest latitudes (Thampi et al. 2016). The downward field-aligned effect of the poleward winds extended the depletion into midlatitudes, and the positive response faded in the evening as the EIA crest was eroded.

LSTIDs are generally regarded as ionospheric manifestations of atmospheric gravity waves excited by high-latitude energy and momentum deposition, which propagate equatorward during geomagnetic

storms (Tsugawa et al. 2003). In this event, high-latitude activity not only drove longer-term thermospheric circulation and background ionospheric changes but also excited disturbances propagating toward low and middle latitudes. Specifically, the integrated FAC in the East Asian sector intensified rapidly after the onset of the main phase and reached two peaks, with local peaks persisting into the early recovery phase and a further strengthening during 07-11 UT, while AE increased several times during the corresponding stages. These enhancement periods were closely linked in time to the occurrence of the five LSTID groups, supporting an association on an event timescale. Given the limited spatial resolution of the integrated FAC and the propagation delay between the source and observation regions, no one-to-one attribution of individual current peaks to individual disturbance groups is attempted here. The alternating positive and negative phases that migrated continuously equatorward in the five events are consistent with the picture in which high-latitude heating and momentum input excite large-scale gravity waves, which then produce propagating electron density disturbances through ion-neutral coupling. Previous studies have documented equatorward-propagating structures following high-latitude activity during geomagnetic storms and regional differences in the East Asian sector (Liu et al. 2019). Analyses of the same storm have also reported a close temporal correspondence between enhanced Joule heating and LSTID occurrence (Xu et al. 2026).

The parameters of the five disturbance groups are consistent with previous statistical results: phase speeds of 397-662 m/s, periods of approximately 50-64 min, and wavelengths of 1380-2383 km, all within the typical range of LSTIDs (Borries et al. 2009; Tsugawa et al. 2004). Notably, the speeds show a correspondence with the intensity of high-latitude activity. G1-G3 (523-662 m/s), which occurred during periods of strong high-latitude energy input, were systematically faster than G4 and G5 (397-403 m/s), which occurred during periods of weaker input. This is consistent with the reported statistical tendency for faster disturbance propagation during stronger auroral current activity (Guerra et al. 2025), providing indirect support for modulation by high-latitude energy input intensity. As mentioned above, G1 (during the rising phase) and G4 (during a low-activity interval) lack a clear preceding FAC peak when only the integrated FAC is considered. However, when AE and IEF Ey are also taken into account, G1 occurred about 1 h after the strong AE enhancement at 15:53 UT on 10 October (approximately 4274 nT), when IEF Ey was undergoing the rapid change associated with Event I (Figure 10), while G4 occurred within a period of enhanced AE activity; both groups remain compatible with the lag-based interpretation when the electrojet indices are considered. Thus, all five disturbance groups can be

incorporated into a unified framework in which high-latitude energy injection excites atmospheric waves that propagate to low and middle latitudes, and the observed lag times are consistent with previously reported timescales for aurorally excited disturbance propagation (Lyons et al. 2019). The speed differences among the groups may reflect source-region structure, background winds, and dissipation conditions (Tsugawa et al. 2003, 2004). However, the available wind information is insufficient to separate their contributions, and the specific propagation paths and source regions of each LSTID group require more complete spatiotemporal constraints.

Conclusions

This study combined multi-source observations from BDS-GEO, CMONOC, Swarm, COSMIC-2, GUVI, AMPERE, and ground-based magnetometers with TIE-GCM simulations to investigate the evolution of positive and negative ionospheric storms and the propagation characteristics of LSTIDs over China during the geomagnetic storm of 10-11 October 2024. The main conclusions are as follows:

(1) From the late main phase to the early recovery phase, a low-latitude positive storm coexisted with negative disturbances at higher latitudes over China, followed by negative-storm dominance. The positive storm, accompanied by enhancement and poleward expansion of the EIA crest, had largely disappeared by approximately 13:00 UT on 11 October. The negative storm was concentrated at 15°-35°N and intensified toward lower latitudes, with maximum VTEC depletions of 51.8 TECU (>60% of the background, persisting for 12.5 h) at KUN1 and 31.8 TECU (6.9 h) at WUH1, whereas no sustained negative storm developed at ULAB. CMONOC observations show that the negative storm formed near 05:00 UT at low latitudes, deepened, and expanded northward, while weak enhancement persisted at 35°-45°N. Swarm and COSMIC-2 observations further confirmed the latitudinal coexistence of positive and negative storms and the transition from early enhancement to deep depletion with an elevated F2 peak.

(2) The evolution of the positive and negative storms was jointly controlled by disturbance electric fields and neutral winds. Nighttime eastward disturbance electric fields and penetration electric fields under undershielding enhanced the fountain effect, while equatorward winds lifted the midlatitude F layer, together producing the early recovery-phase positive storm. During daytime, the disturbance electric field turned westward, suppressing the fountain effect

and driving downward plasma drifts; together with the downward effect of poleward winds, this led to the negative storm. The two-station H-component magnetic difference, TIE-GCM wind fields, and GUVI O/N_2 observations support the roles of the daytime westward disturbance electric field, poleward winds, and the limited contribution of thermospheric compositional depletion.

(3) Five groups of equatorward-propagating LSTIDs were identified during the storm, including two during the main phase and three during the recovery phase, with phase speeds of 397-662 m/s, periods of 50-64 min, and wavelengths of 1380-2383 km. Their occurrence corresponded, on an event timescale, to enhancements of integrated FAC in the East Asian sector and AE activity. The three groups during periods of stronger high-latitude energy input propagated systematically faster than the two groups during weaker-input periods, supporting atmospheric gravity waves excited by auroral heating and momentum input as their common source. Penetration electric fields may have mainly modulated the background ionospheric state rather than directly triggering the individual LSTID groups.

Acknowledgements

The authors thank the China Earthquake Networks Center, the Crustal Movement Observation Network of China, and the International GNSS Service (https://igs.org/) for providing GNSS data support. The associated GNSS data are available from the National Earthquake Data Center, while BDS-GEO observations were obtained from the Multi-GNSS Experiment (https://network.igs.org/) and the International GNSS Monitoring and Assessment System (http://www.igmas.org/). Geomagnetic observations were obtained from INTERMAGNET (https://www.intermagnet.org/). Solar wind parameters and geomagnetic indices were obtained from the NASA OMNIWeb database (https://omniweb.gsfc.nasa.gov/). Field-aligned current and thermospheric composition data were obtained from the AMPERE (https://ampere.jhuapl.edu/) and TIMED/GUVI (https://guvitimed.jhuapl.edu/) teams at the Johns Hopkins University Applied Physics Laboratory, respectively. COSMIC-2 electron density profiles were provided by the UCAR COSMIC Program (https://www.cosmic.ucar.edu/what-we-do/cosmic-2/). Swarm data were provided by the European Space Agency (https://swarm-diss.eo.esa.int/). TIE-GCM simulations were performed using the community model developed at the National Center for Atmospheric Research (https://www.hao.ucar.edu/

modeling/tgcm).

Funding

This work was supported by the Key Program of the National Natural Science Foundation of China (42330105) and the Discipline Breakthrough Pilot Project (JYB2025XDXM111).

Competing interests

The authors declare that they have no competing interests.

References

Anderson BJ, Korth H, Waters CL, Green DL, Merkin VG, Barnes RJ, Dyrud LP (2014) Development of large-scale Birkeland currents determined from the Active Magnetosphere and Planetary Electrodynamics Response Experiment. Geophys Res Lett 41:3017-3025. https://doi.org/10.1002/2014GL059941

Anderson D, Anghel A, Yumoto K, Ishitsuka M, Kudeki E (2002) Estimating daytime vertical E×B drift velocities in the equatorial F-region using ground-based magnetometer observations. Geophys Res Lett 29:1596. https://doi.org/10.1029/2001GL014562

Astafyeva E, Zakharenkova I, Förster M (2015) Ionospheric response to the 2015 St. Patrick's Day storm: a global multi-instrumental overview. J Geophys Res Space Phys 120:9023-9037. https://doi.org/10.1002/2015JA021629

Bagiya MS, Iyer KN, Joshi HP, Thampi SV, Tsugawa T, Ravindran S et al (2011) Low-latitude ionospheric-thermospheric response to storm time electrodynamical coupling between high and low latitudes. J Geophys Res Space Phys 116:A01303. https://doi.org/10.1029/2010JA015845

Balan N, Alleyne H, Otsuka Y, Vijaya Lekshmi D, Fejer BG, McCrea I (2009) Relative effects of electric field and neutral wind on positive ionospheric storms. Earth Planets Space 61:439-445. https://doi.org/10.1186/BF03353160

Balan N, Shiokawa K, Otsuka Y, Kikuchi T, Vijaya Lekshmi D, Kawamura S et al (2010) A physical mechanism of positive ionospheric storms at low latitudes and midlatitudes. J Geophys Res Space Phys 115:A02304. https://doi.org/10.1029/2009JA014515

Blanc M, Richmond AD (1980) The ionospheric disturbance dynamo. J Geophys Res Space Phys 85:1669-1686. https://doi.org/10.1029/JA085iA04p01669

Borries C, Jakowski N, Wilken V (2009) Storm induced large scale TIDs observed in GPS derived TEC. Ann Geophys 27:1605-1612. https://doi.org/10.5194/angeo-27-1605-2009

Buonsanto MJ (1999) Ionospheric storms—a review. Space Sci Rev 88:563-601. https://doi.org/10.1023/A:1005107532631

Christensen AB, Paxton LJ, Avery S, Craven J, Crowley G, Humm DC et al (2003) Initial observations with the Global Ultraviolet Imager (GUVI) in the NASA TIMED satellite mission. J Geophys Res Space Phys 108:1451. https://doi.org/10.1029/2003JA009918

Ding F, Wan W, Ning B, Wang M (2007) Large-scale traveling ionospheric disturbances observed by GPS total electron content during the magnetic storm of 29-30 October 2003. J Geophys Res Space Phys 112:A06309. https://doi.org/10.1029/2006JA012013

Ding F, Wan W, Ning B, Zhao B, Li Q, Zhang R et al (2012) Two-dimensional imaging of l

arge-scale traveling ionospheric disturbances over China based on GPS data. J Geophys Res Space Phys 117:A08318. https://doi.org/10.1029/2012JA017546

Fejer BG (2002) Low latitude storm time ionospheric electrodynamics. J Atmos Sol Terr Phys 64:1401-1408. https://doi.org/10.1016/S1364-6826(02)00103-7

Fejer BG (2011) Low latitude ionospheric electrodynamics. Space Sci Rev 158:145-166. https://doi.org/10.1007/s11214-010-9690-7

Fejer BG, Jensen JW, Su S-Y (2008) Seasonal and longitudinal dependence of equatorial disturbance vertical plasma drifts. Geophys Res Lett 35:L20106. https://doi.org/10.1029/2008GL035584

Fuller-Rowell TJ, Codrescu MV, Rishbeth H, Moffett RJ, Quegan S (1996) On the seasonal response of the thermosphere and ionosphere to geomagnetic storms. J Geophys Res Space Phys 101:2343-2353. https://doi.org/10.1029/95JA01614

Guerra M, Cesaroni C, Fiorentino N, Tosone F, Ventriglia V, Pica E et al (2025) Automatic detection of large-scale traveling ionospheric disturbances using GNSS data and image processing techniques. Space Weather 23:e2025SW004423. https://doi.org/10.1029/2025SW004423

Hocke K, Schlegel K (1996) A review of atmospheric gravity waves and travelling ionospheric disturbances: 1982-1995. Ann Geophys 14:917-940. https://doi.org/10.1007/s00585-996-0917-6

Hunsucker RD (1982) Atmospheric gravity waves generated in the high-latitude ionosphere: a review. Rev Geophys 20:293-315. https://doi.org/10.1029/RG020i002p00293

Kataoka R, Nakano S, Uchino S, Reddy SA (2025) Extended red aurora associated with supersubstorm igniting the October 10, 2024 magnetic storm as revealed by citizen science. Earth Planets Space 77:64. https://doi.org/10.1186/s40623-025-02178-w

Krypiak-Gregorczyk A, Wielgosz P (2018) Carrier phase bias estimation of geometry-free linear combination of GNSS signals for ionospheric TEC modeling. GPS Solut 22:45. https://doi.org/10.1007/s10291-018-0711-4

Liu J, Zhang D-H, Coster AJ, Zhang S-R, Ma G-Y, Hao Y-Q, Xiao Z (2019) A case study of the large-scale traveling ionospheric disturbances in the eastern Asian sector during the 2015 St. Patrick's Day geomagnetic storm. Ann Geophys 37:673-687. https://doi.org/10.5194/angeo-37-673-2019

Lu G, Goncharenko LP, Richmond AD, Roble RG, Aponte N (2008) A dayside ionospheric positive storm phase driven by neutral winds. J Geophys Res Space Phys 113:A08304. https://doi.org/10.1029/2007JA012895

Lyons LR, Nishimura Y, Zhang S-R, Coster AJ, Bhatt A, Kendall E, Deng Y (2019) Identification of auroral zone activity driving large-scale traveling ionospheric disturbances. J Geophys Res Space Phys 124:700-714. https://doi.org/10.1029/2018JA025980

Mendillo M (2006) Storms in the ionosphere: patterns and processes for total electron content. Rev Geophys 44:RG4001. https://doi.org/10.1029/2005RG000193

Paul KS, Haralambous H, Moses M, Tripathi SC (2025) Effects of the October 2024 storm over the global ionosphere. Remote Sens 17:2329. https://doi.org/10.3390/rs17132329

Pierrard V, Verhulst TGW, Chevalier J-M, Bergeot N, Winant A (2025) Effects of the geomagnetic superstorms of 10-11 May 2024 and 7-11 October 2024 on the ionosphere and plasmasphere. Atmosphere 16:299. https://doi.org/10.3390/atmos16030299

Qian L, Burns AG, Emery BA, Foster B, Lu G, Maute A et al (2014) The NCAR TIE-GCM:

a community model of the coupled thermosphere/ionosphere system. In: Huba JD, Schunk RW, Khazanov GV (eds) Modeling the ionosphere-thermosphere system. Wiley, pp 73-83. https://doi.org/10.1002/9781118704417.ch7

Rai D, Tulasi Ram S, Nilam B, Oliveira DM, Remya B, Raghav A et al (2026) Dawn-side anomaly in sudden geomagnetic field responses to solar wind pressure discontinuities during the 10 May and 10 October 2024 geomagnetic storms. Geophys Res Lett 53:e2025GL119914. https://doi.org/10.1029/2025GL119914

Scherliess L, Fejer BG (1997) Storm time dependence of equatorial disturbance dynamo zonal electric fields. J Geophys Res Space Phys 102:24037-24046. https://doi.org/10.1029/97JA02165

Singh R, Scipión DE, Kuyeng K, Condor P, Flores R, Pacheco E et al (2025) Ionospheric responses to an extreme (G5-level) geomagnetic storm using multi-instrument measurements at the Jicamarca Radio Observatory on 10-11 October 2024. J Geophys Res Space Phys 130:e2024JA033642. https://doi.org/10.1029/2024JA033642

Sun Y, Tang J, Teng H, Xu C, Zhang L (2026) Analysis of ionospheric disturbances near 120° E in the Asia-Pacific sector during the May 2024 superstorm using multi-instrument observations. Space Weather 24:e2025SW004805. https://doi.org/10.1029/2025SW004805

Thampi SV, Shreedevi PR, Choudhary RK, Pant TK, Chakrabarty D, Sunda S et al (2016) Direct observational evidence for disturbance dynamo on the daytime low-latitude ionosphere: a case study based on the 28 June 2013 space weather event. J Geophys Res Space Phys 121:10064-10074. https://doi.org/10.1002/2016JA023037

Tsugawa T, Saito A, Otsuka Y, Yamamoto M (2003) Damping of large-scale traveling ionospheric disturbances detected with GPS networks during the geomagnetic storm. J Geophys Res Space Phys 108:1127. https://doi.org/10.1029/2002JA009433

Tsugawa T, Saito A, Otsuka Y (2004) A statistical study of large-scale traveling ionospheric disturbances using the GPS network in Japan. J Geophys Res Space Phys 109:A06302. https://doi.org/10.1029/2003JA010302

Tsurutani B, Mannucci A, Iijima B, Abdu MA, Sobral JHA, Gonzalez W et al (2004) Global dayside ionospheric uplift and enhancement associated with interplanetary electric fields. J Geophys Res Space Phys 109:A08302. https://doi.org/10.1029/2003JA010342

Veenadhari B, Alex S, Kikuchi T, Shinbori A, Singh R, Chandrasekhar E (2010) Penetration of magnetospheric electric fields to the equator and their effects on the low-latitude ionosphere during intense geomagnetic storms. J Geophys Res Space Phys 115:A03305. https://doi.org/10.1029/2009JA014562

Xu C, Wang J, Tang J, Hu M (2026) Electric field and thermospheric control of recovery-phase TEC and ionospheric irregularities over China during the May and October 2024 G5 superstorms. J Geophys Res Space Phys 131:e2026JA035227. https://doi.org/10.1029/2026JA035227